analytical chemistry

pubs.acs.org/ac

Article

Highly Efficient Electrochemiluminescence Based on Luminol/MoS_2 Quantum Dots@Zeolitic Imidazolate Framework-8 as an Emitter for Ultrasensitive Detection of MicroRNA

Wei Liu, Meiling Su, Anyi Chen, Kanfu Peng, Yaqin Chai,* and Ruo Yuan*

Cite This: *Anal. Chem.* 2022, 94, 9106−9113

Read Online

ACCESS | Metrics & More | Article Recommendations | Supporting Information

ABSTRACT: Herein, a highly efficient electrochemiluminescence (ECL) emitter, luminol/MoS_2 quantum dots@zeolitic imidazolate framework-8 (Lu/MoS_2 QDs@ZIF-8), with a positive charge was prepared to construct a novel luminol−H_2O_2−MoS_2 QD ternary ECL system for ultrasensitive detection of microRNA-21 (miRNA-21). The porous Lu/MoS_2 QDs@ZIF-8 was beneficial for reducing the accessible distance between various participants in the ternary system wherein co-reaction accelerator MoS_2 QDs promoted H_2O_2 to generate superoxide anion radicals ($O_2^{\bullet-}$), which instantaneously reacted with luminol to produce robust ECL signals. Simultaneously, the positively charged Lu/MoS_2 QDs@ZIF-8 facilitated the enrichment of $O_2^{\bullet-}$ to further improve the ECL efficiency of luminol. Impressively, compared with the traditional binary luminol−H_2O_2 system, the ECL efficiency of this ternary system was increased by 12.7 times. In the aid of a target-cycled and endogenous adenosine triphosphate-driven signal amplification strategy, the biosensor with Lu/MoS_2 QDs@ZIF-8 as an ECL emitter achieved ultrasensitive detection for miRNA-21 with a detection limit of 14.6 aM. This work provides a promising perspective to construct a highly efficient ECL ternary system for biomolecule detection and potential disease diagnosis.

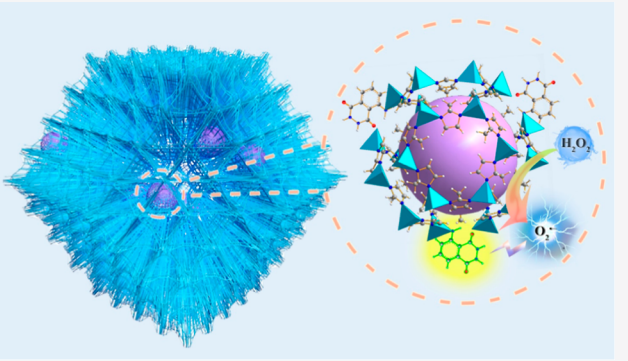

INTRODUCTION

Electrochemiluminescence (ECL), with merits of high sensitivity, low background noise, and instrumentation requirement, has attracted extensive attention in analytical methodology.[1−3] As a classical ECL material, luminol has been widely studied on account of its hypotoxicity and strong ECL emission to construct a binary luminol−H_2O_2 system for detecting RNA,[4,5] DNA,[6,7] and metal ions.[8,9] However, under a specific voltage, the luminol−H_2O_2 system is unable to provide a sufficient ECL efficiency for growing sensitive detection requirements. Taking this into account, amino-modified 3,4,9,10-perylenetetracarboxylic dianhydride,[10] single-atom catalysis,[11,12] metallic oxide,[13,14] and hemin-based DNA biomaterials[15] were successively proposed as co-reaction accelerators to generate more intermediate superoxide anion radicals ($O_2^{\bullet-}$) for highly efficient ECL emission of the luminol−H_2O_2 system. However, the long interaction distance between the luminophore and the co-reaction accelerator and the arbitrary diffusion of extremely short-lived free radicals in the unprotected mode caused unavoidable energy loss to some extent, which impeded the ECL efficiency. Therefore, it was of great significance to construct a new ternary system that shortens the distance between various reactive participants to improve the ECL efficiency.

Recently, metal−organic frameworks (MOFs) have attracted growing interest due to their excellent structural properties and functionality.[16−19] Notably, with multiple combinations of central ion and organic linkers endowing superior tailorability and densely staggered channels providing confined space and protection, MOFs thus exhibited similar structural functions with microreactors[20] Naturally, the narrow chemical environment in the skeleton of MOFs allowed efficient free-radical reaction, indicating superexcellent potential as a response framework, to effectively deal with the obstacle of the loss of $O_2^{\bullet-}$ in a nonexpected manner. Herein, luminol/MoS_2 quantum dots@zeolitic imidazolate framework-8 (Lu/MoS_2 QDs@ZIF-8), an MOFs integrated with luminol and molybdenum disulfide quantum dots (MoS_2 QDs), was prepared, in which luminol as a luminophor and MoS_2 QDs as a co-reaction accelerator were used to improve the ECL efficiency of the luminol−H_2O_2 system. Conspicuously, thanks to the confined space of the cavity microenvironment in ZIF-8

Received: April 2, 2022
Accepted: June 3, 2022
Published: June 15, 2022

https://doi.org/10.1021/acs.analchem.2c01444
Anal. Chem. 2022, 94, 9106−9113

Scheme 1. (A) Preparation of Lu/MoS_2 QDs@ZIF-8; (B) Ultrasensitive Detection Process of the Proposed Biosensor to miRNA-21

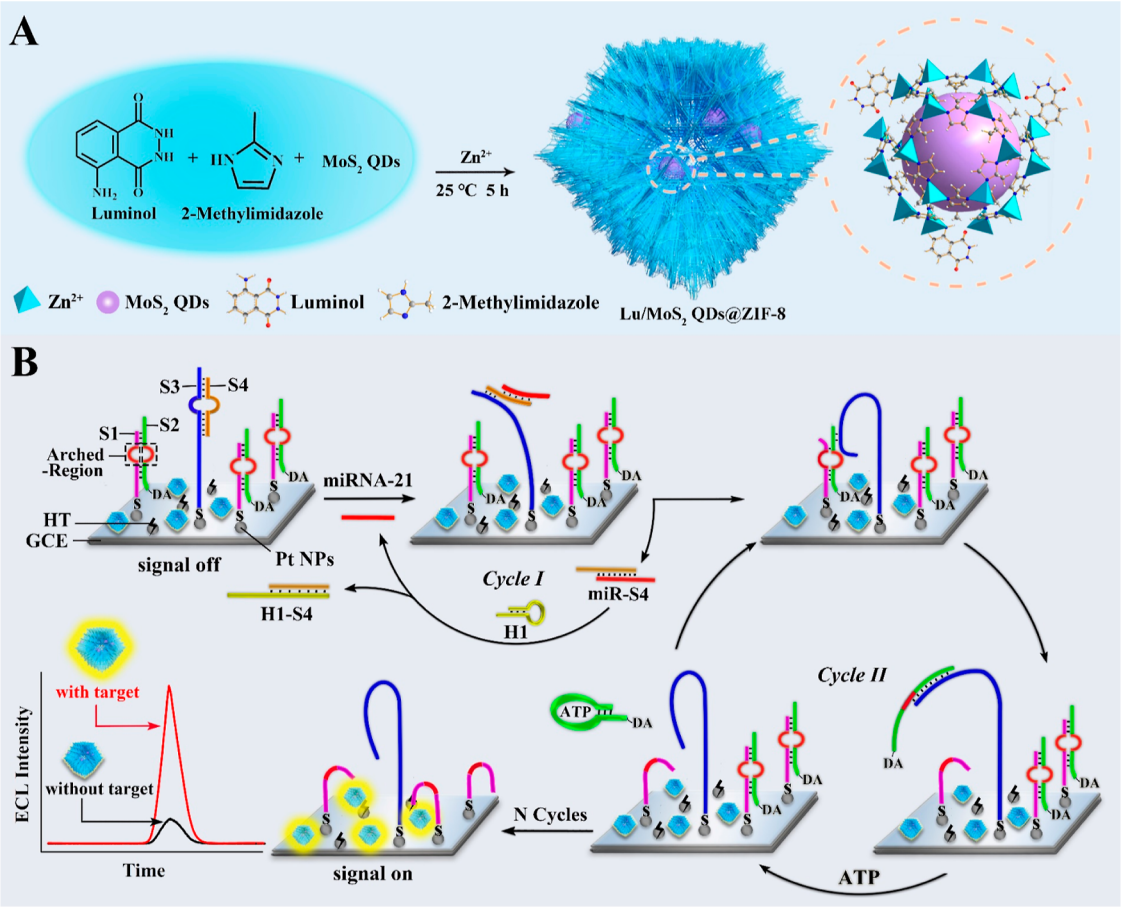

acting as a response framework for reducing the distance between luminol and MoS_2 QDs, a large amount of $O_2^{\bullet-}$ produced by H_2O_2 under the promotion of MoS_2 QDs could rapidly react with luminol in a shortcut path to significantly improve the ECL efficiency. At the same time, the positively charged Lu/MoS_2 QDs@ZIF-8 was prone to enrich more $O_2^{\bullet-}$ to further improve the ECL efficiency.

At present, strategies for efficient signal amplification of microRNA based on a DNA walker machine have been gradually focused due to its eminent cycling activity and controllability.[21−23] Especially, in order to avoid the restriction of using enzymes which commonly required a specific ion concentration and temperature, researchers developed nucleic acid amplification methods that utilized endogenous adenosine triphosphate (ATP) as an optional driving force to trace microRNA.[24−26] Even so, these strategies activated these DNA walkers by sacrificing target microRNA in equal proportion, which resulted in a low converting efficiency, thus limiting the effective signal amplification. In this work, on the basis of ATP as a driving fuel, an arched DNA structure integrating the ATP aptamer and the microRNA-21 (miRNA-21)-associated sequence was reasonably designed to fabricate the coordinated DNA molecular machine, realizing the recycling of target miRNA-21 to enhance the signal amplification efficiency.

Herein, with Lu/MoS_2 QDs@ZIF-8 as an ECL emitter and the target renewable ATP-based DNA walker strategy as a nucleic acid amplification platform, a biosensor was constructed to achieve ultrasensitive detection of miRNA-21. As illustrated in Scheme 1A, Lu/MoS_2 QDs@ZIF-8 was prepared by the amino of luminol coordinating with zinc ions and the in situ encapsulation of MoS_2 QDs in ZIF-8. Then, Lu/MoS_2 QDs@ZIF-8 and platinum nanoparticles (Pt NPs) were immobilized on the interface of the glassy carbon electrode (GCE) (Scheme 1B). Additionally, the duplex DNA S1−S2 and S3−S4 were prepared, wherein S2 contained the aptamer sequence of ATP which was blocked by S1 and the terminal of S2 was modified with dopamine (DA), which could quench the ECL signal of luminol; simultaneously, S3 acted as a DNA swing walker which was blocked by S4. After incubation of S1−S2 and S3−S4, the ECL signal of the biosensor was drastically quenched in the initial state (signal off). When the target miRNA-21 existed, S4 was captured by miRNA-21 through the arched regions and formed duplex miR-S4. Furthermore, hairpin DNA (H1) hybridized with miR-S4 via the sticky end and displaced miRNA-21 to achieve the recycling of the target. When S3 captured S2 through branching migration reaction, S2 quickly formed a complex with ATP to escape from GCE, which caused the recovery of the ECL signal (signal on) and the recycling of S3. Through target regeneration and continuous ATP-driven cycling, a very small amount of miRNA-21 triggered evident ECL signal response. Significantly, the biosensor achieved ultrasensitive detection of miRNA-21 with a detection limit of 14.6 aM. This work not only presents a universal strategy for enhancing the ECL efficiency of the ternary system but also shows broad

https://doi.org/10.1021/acs.analchem.2c01444
Anal. Chem. 2022, 94, 9106−9113

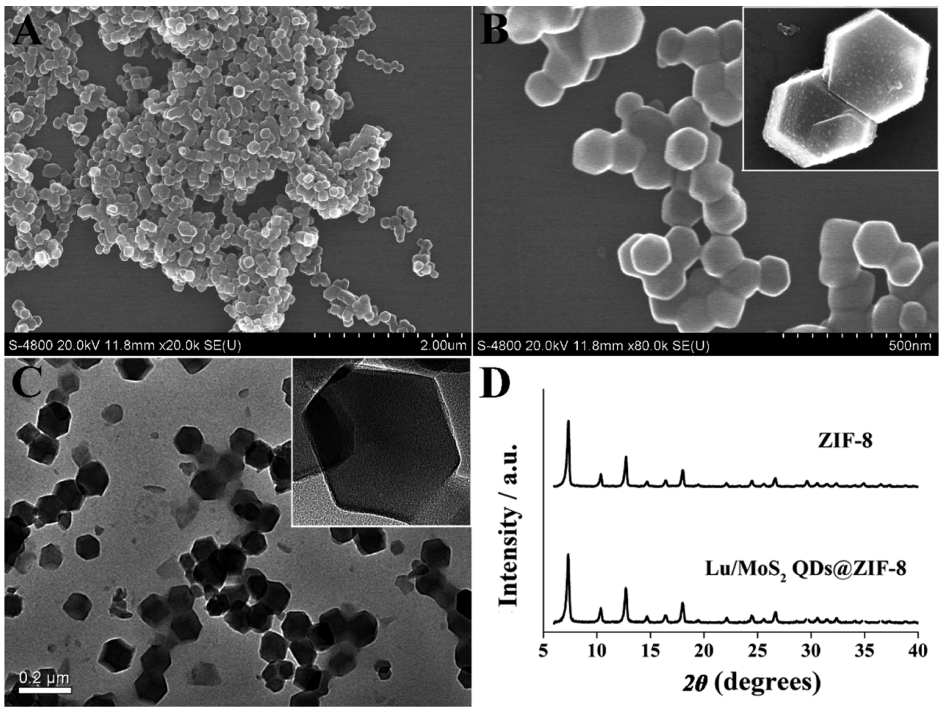

Figure 1. (A,B) SEM and (C) TEM images of Lu/MoS_2 QDs@ZIF-8. (D) XRD pattern of ZIF-8 and Lu/MoS_2 QDs@ZIF-8.

practical application prospects in ultrasensitive detection of biomarkers and timely diagnosis of early-stage cancer.

EXPERIMENTAL SECTION

Synthesis of MoS_2 QDs. Briefly, 0.25 g of bulk molybdenum disulfide powder was added into 25 mL of DMF. Followed by continuous sonication for 24 h, the resultant mixture above was refluxed with gentle stirring for 6 h at 140 °C. Next, the solution was treated with ultrasound for another 2 h and then centrifuged at 8000 rpm to collect the yellow supernatant. Later, prepared MoS_2 QDs were dialyzed against deionized water for 48 h to obtain the MoS_2 QD aqueous solution.

Synthesis of Lu/MoS_2 QDs@ZIF-8, MoS_2 QDs@ZIF-8, and Lu@ZIF-8. 0.1 mL of luminol (0.1 M in 0.01 M NaOH), 4.0 mL of zinc nitrate solution (0.05 M in methanol), 5.5 mL of 2-methyl imidazole (1.2 M in methanol), and 0.4 mL of MoS_2 QD solution were mixed with stirring for 5 h. Sequentially, after standing for 5 h, the nanocomposites were obtained by alternative centrifuging and washing three times with deionized water and methanol. Finally, Lu/MoS_2 QDs@ZIF-8 was redissolved in 5.0 mL of methanol for subsequent detection operations. The preparation processes of MoS_2 QD encapsulated zeolitic imidazolate framework-8 (MoS_2 QDs@ZIF-8) and luminol-coordinated ZIF-8 (Lu@ZiF-8) were identical to that of Lu/MoS_2 QDs@ZIF-8 while there was no addition of luminol and MoS_2 QDs, respectively.

Preparation of the Proposed Biosensor. Initially, GCE was processed by sonication and scouring to obtain a mirror interface. Subsequently, 10 μL of the luminous substrate obtained by the mixture of Lu/MoS_2 QDs@ZIF-8, Pt nanoparticles, and chitosan solution (10 mL, 0.01%, w/w) in a volume ratio of 1:1:8 was dropped on GCE and then dried at 80 °C for 3 h to form a luminescent layer. Additionally, 10 μL of a mixed solution containing double-stranded S1−S2 (2.0 μM) and S3−S4 (0.2 μM) was incubated on the luminescent layer at 4 °C for 10 h. After washing with deionized water, the resultant electrodes were processed with 10 μL of hexanethiol (1.0 mM) for 50 min to seal nonspecific adsorption sites. Finally, the biosensors were stored at 4 °C for subsequent usage.

Measurement Procedure. 10 μL of a mixture containing hairpin DNA (H1, 0.3 μM), ATP (0.1 mM), and a specific concentration of miRNA-21 was dropped on as-prepared biosensors, which were further placed at 37 °C for 80 min. After that, the biosensors were rinsed adequately with deionized water and ECL measurements were implemented in a way that biosensors were severally immersed in 0.1 M phosphate-buffered saline (PBS, pH 7.4) containing 2.0 mM H_2O_2 with a scanning potential of 0−0.6 V and a scanning speed of 0.1 V/s.

RESULTS AND DISCUSSION

Characterization for Prepared Nanomaterials. Morphologic investigation for prepared nanomaterials was performed through scanning electron microscopy (SEM) and transmission electron microscopy (TEM). With constituents of zinc ions and 2-methylimidazole in the precursor, ZIF-8 showcased a polyhedral structure[27] (Figure S1). Compared to pristine ZIF-8 with an average particle size of 50 nm, the particle size of Lu/MoS_2 QDs@ZIF-8 was increased to 80−120 nm with a slightly rough surface after the immobilization of MoS_2 QDs and luminol (Figure 1A,B). TEM imaging (Figure 1C) and atomic force microscopy imaging (Figure S2) further proved the morphological properties of Lu/MoS_2 QDs@ZIF-8. Additionally, X-ray diffraction (XRD) was carried out to study the crystalline nature of ZIF-8 and Lu/MoS_2 QDs@ZIF-8 (Figure 1D). The XRD plots obtained from Lu/MoS_2 QDs@ZIF-8 showed a coincident flat baseline corresponding to that of ZIF-8, revealing that the introduction of luminol and MoS_2 QDs hardly altered the crystal structure of ZIF-8.

https://doi.org/10.1021/acs.analchem.2c01444
Anal. Chem. 2022, 94, 9106−9113

Fourier transform infrared spectroscopy (FTIR) was employed to investigate the coordination process of luminol with ZIF-8. As displayed in Figure 2A, the spectrum of pure luminol was first depicted, where the robust peak at 1657 cm^{-1} was attributed to the C═O stretch vibrational band, a secondary structure of the amide I region.[28] At the same time, the classical peak of $-NH_2$ at 1303 cm^{-1} was attributed to aniline in luminol. The fingerprint characteristic peaks of benzene were observed at 815 and 702 cm^{-1}. When luminol was involved in Lu/MoS_2 QDs@ZIF-8, a strong peak was found at 1660 cm^{-1}, indicating the presence of C═O. However, a peak shift occurred at 1315 cm^{-1}, possibly attributed to the N−H distortion in luminol covalent grafting.[29] Similarly, the fingerprint characteristic peak of benzene moved correspondingly to a low wave frequency. Therefore, it could be concluded that the binding of luminol to ZIF-8 was achieved by the coordination of the amine group with the zinc ion. Subsequently, ECL assay for MoS_2 QD encapsulated ZIF-8 (MoS_2 QDs@ZIF-8) and Lu/MoS_2 QDs@ZIF-8 was also performed. Figure 2B shows that MoS_2 QDs@ZIF-8 revealed no response with the change of applied voltage, while Lu/MoS_2 QDs@ZIF-8 exhibited a strong ECL peak, confirming the successful immobilization of luminol. In addition, the immobilization efficiency of luminol was calculated to be 25.5% (Figure S3).

To verify the scientific nature of achieving the encapsulation of MoS_2 QDs, N_2 adsorption/desorption isotherm and pore size distribution studies of Lu/MoS_2 QDs@ZIF-8 and morphology characterization of MoS_2 QDs were performed.

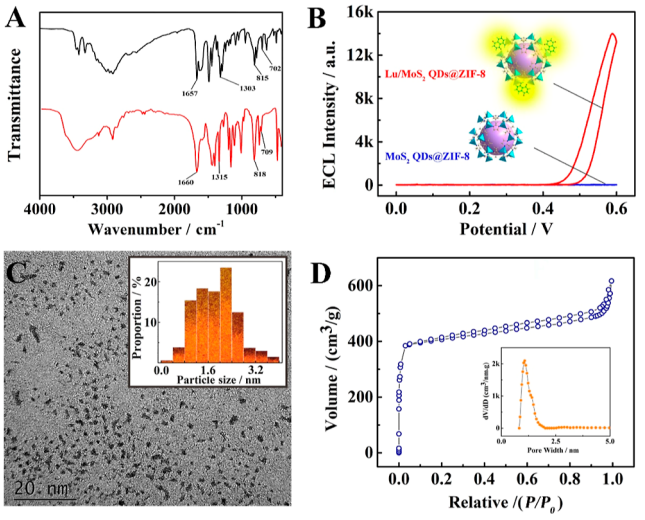

Figure 2. (A) FTIR spectra of luminol (in black) and Lu/MoS_2 QDs@ZIF-8 (in red). (B) ECL response for MoS_2 QDs@ZIF-8 and Lu/MoS_2 QDs@ZIF-8. (C) TEM image (inset: size distribution) of MoS_2 QDs. (D) BET characterization of Lu/MoS_2 QDs@ZIF-8.

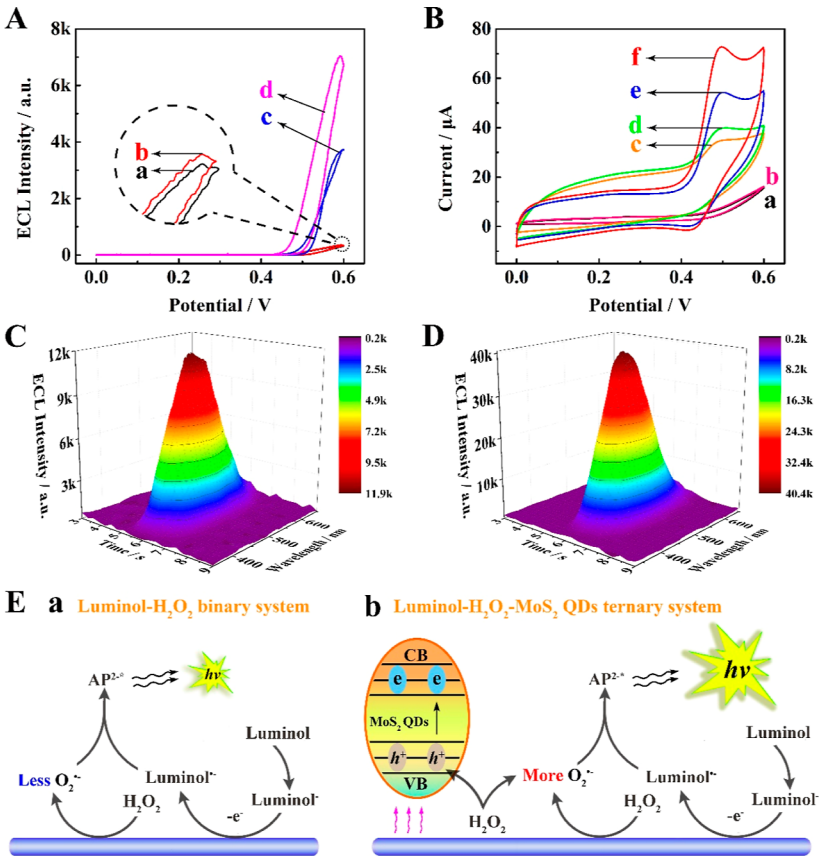

Figure 3. (A) ECL responses of GCE in PBS (0.1 M, pH 7.4) containing (a) luminol (50 μM) and (c) luminol (50 μM) and H_2O_2 (2.0 mM); ECL responses of MoS_2 QDs/GCE in PBS containing (b) luminol (50 μM) and (d) luminol (50 μM) and H_2O_2 (2.0 mM). (B) CV curves of GCE in PBS containing (a) luminol (50 μM), (c) H_2O_2 (2.0 mM), and (e) luminol (50 μM) and H_2O_2 (2.0 mM) and MoS_2 QDs/GCE in PBS containing (b) luminol (50 μM), (d) H_2O_2 (2.0 mM), and (f) luminol (50 μM) and H_2O_2 (2.0 mM). Spooled ECL spectra of (C) luminol (50 μM) and (D) Lu/MoS_2 QDs@ZIF-8. (E) Inferences on the reaction mechanisms of (a) binary luminol−H_2O_2 system and (b) ternary luminol−H_2O_2−MoS_2 QDs system.

https://doi.org/10.1021/acs.analchem.2c01444
Anal. Chem. 2022, 94, 9106−9113

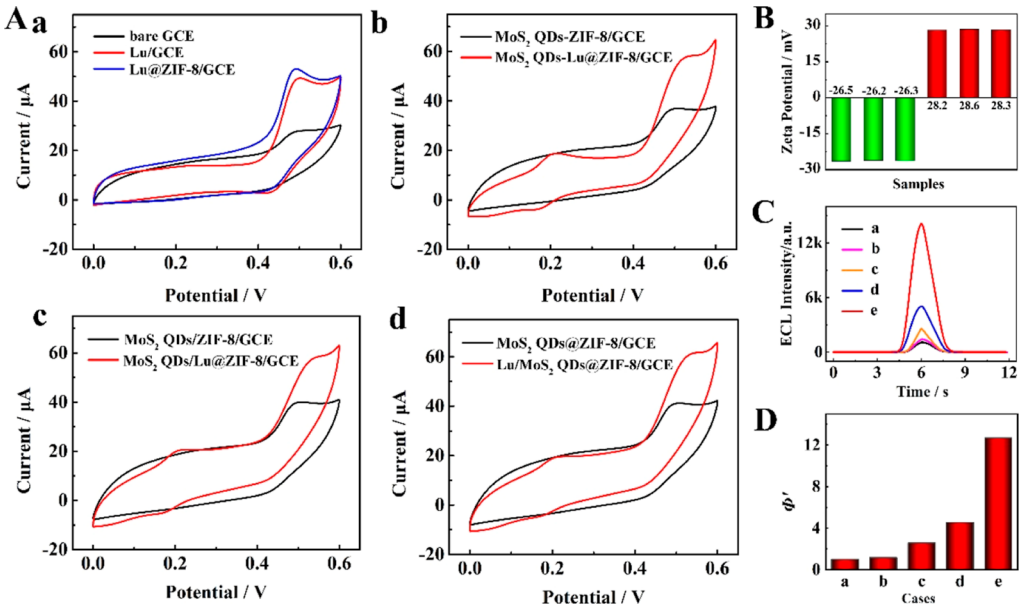

Figure 4. (A) CV curves of (a) bare GCE, Lu/GCE, and Lu@ZIF-8/GCE in PBS containing 2.0 mM H_2O_2; CV curves of (b) MoS_2 QDs−ZIF-8/GCE (ZIF-8-modified GCE in PBS containing MoS_2 QDs and 2.0 mM H_2O_2) and MoS_2 QDs/Lu@ZIF-8/GCE (Lu@ZIF-8/GCE in PBS containing MoS_2 QDs and 2.0 mM H_2O_2); CV curves of (c) MoS_2 QDs/ZIF-8/GCE (MoS_2 QDs were filmed on the surface of ZIF-8/GCE) and MoS_2 QDs/Lu@ZIF-8/GCE (MoS_2 QDs were filmed on the surface of Lu@ZIF-8/GCE) in PBS containing 2.0 mM H_2O_2; CV curves of (d) MoS_2 QDs@ZIF-8/GCE (MoS_2 QD-embedded ZIF-8 was filmed on the surface of GCE) and Lu/MoS_2 QDs@ZIF-8/GCE in PBS containing 2.0 mM H_2O_2. (B) ζ potential of luminol (in green) and MoS_2 QDs@ZIF-8 (in red) under three parallel experiments. (C) ECL responses and (D) relative ECL efficiency of luminol in different cases: (a) Lu/GCE, (b) Lu@ZIF-8/GCE, (c) MoS_2 QDs/Lu@ZIF-8/GCE, (d) MoS_2 QDs/Lu@ZIF-8/GCE, and (e) Lu/MoS_2 QDs@ZIF-8/GCE.

As shown in Figures 2C and S4, the particle size of MoS_2 QDs was mostly distributed at 1.2 to 2.8 nm. Brunauer−Emmett−Teller (BET) revealed that the average pore size of Lu/MoS_2 QDs@ZIF-8 was 1.07 nm with a high specific surface area of 1724 $m^2 \cdot g^{-1}$, demonstrating theoretically feasible encapsulation capability toward to MoS_2 QDs (Figure 2D). Next, high-resolution TEM and energy-dispersive X-ray (EDX) mapping for Lu/MoS_2 QDs@ZIF-8 were carried out, and the results are displayed in Figures S5 and S6. As illustrated in Figure S5D, an ordered and parallel lattice fringe with a *d*-spacing of 0.23 nm was noticed, which was in accord with the (103) faces of MoS_2 well crystals.[30,31] Conspicuously, the uniform distribution of each element in EDX mapping images proved the successful encapsulation of MoS_2 QDs, which was consistent with the speculation of BET and confirmed the feasibility nature of the assembly strategy, and the immobilization efficiency of MoS_2 QDs was calculated to be 16.2% (Figures S7 and S8).

Exploration of the Possible Reaction Mechanism. In order to ascertain the interaction mechanism of the ternary luminol−H_2O_2−MoS_2 QDs system, ECL and cyclic voltammetry (CV) characterization were implemented. Figure 3A shows that when PBS (0.1 M, pH 7.4) contains only 50 μM luminol, bare GCE and MoS_2 QD-modified GCE (MoS_2 QDs/GCE) only showed similar low ECL signals. However, when both luminol and H_2O_2 (2.0 mM) were contained in PBS (0.1 M, pH 7.4), the ECL emission of bare GCE and MoS_2 QDs/GCE was significantly enhanced, and the ECL intensity of MoS_2 QDs/GCE was significantly higher than that of bare GCE. This promotion behavior was consistent with the concept of the co-reaction accelerator in the recently reported ternary system.[32] Therefore, as shown in Figures 3B and S9, additional CV characterization was performed and demonstrated the promotion property of MoS_2 QDs. Spooled ECL assay was performed to track evolution and devolution of luminol and Lu/MoS_2 QDs@ZIF-8 (Figure 3C,D). Throughout the potential cycle, the ECL peak wavelength of Lu/MoS_2 QDs@ZIF-8 was consistent with that of luminol, indicating that only one excited state existed in the reaction system. Therefore, it was determined that luminol was the only illuminant in the system. In addition, according to Randles−Sevcik equation (eq S3), the ratio of the relative electrochemical surface area of Lu/MoS_2 QDs@ZIF-8-modified GCE to that of luminol-modified GCE was 1.26 (Figure S10). It was impressive to find that Lu/MoS_2 QDs@ZIF-8 increased the effective electrochemical surface area of GCE to a considerable extent for enhancing the ECL signal.

Based on the results of the above experiment and previous works, possible reaction mechanisms of the luminol−H_2O_2−MoS_2 QDs system are summarized in Figure 3E. First, $O_2^{\bullet-}$ was produced through electrocatalysis of H_2O_2 at the surface of GCE. Simultaneously, applied voltage triggered the electrochemical oxidation of luminol$^{\bullet-}$, which further reacted with $O_2^{\bullet-}$ generating high-activity 3-aminophthalate (AP^{2-}*). Then, the generated AP^{2-}* converted to the ground state accompanying photon emission. It was noteworthy that ZIF-8 and MoS_2 QDs enriched the generation pathway of $O_2^{\bullet-}$. Excited by applied potential, the electrons in the valence band of MoS_2 QDs shuttled to the conduction band acting as charge carriers and then traveled to GCE with the generation of electron holes (h^+). Electronic coupling between the valence band of MoS_2 QDs and the molecular orbital of H_2O_2 was instantaneously triggered in interspace compact and delivery accessible electroactivity interior of ZIF-8 with the generation of $O_2^{\bullet-}$. Therefore, more $O_2^{\bullet-}$ was generated in the super-enhanced luminol−H_2O_2−MoS_2 QDs system to promptly react with luminol$^{\bullet-}$, leading to an improved ECL efficiency.

https://doi.org/10.1021/acs.analchem.2c01444
Anal. Chem. 2022, 94, 9106−9113

Relative ECL Efficiency of Different Composites. To accurately calculate the relative ECL efficiency (Φ'), the difference in the CV curve and ECL response was recorded via the characterization of GCE modified with different materials. Lu/GCE was prepared as a standard to calculate the relative ECL efficiency of luminol in different nanocomposites. Figure 4A shows that after luminol was doped into ZIF-8 alone (Lu@ZIF-8), there was no significant current difference, so the calculated current integral difference was not obvious (from 3.81×10^{-5} to 3.94×10^{-5} C). Next, we explored the current and ECL variation when MoS_2 QDs were dispersed into the detection substrate, modified to the exterior and interior of Lu@ZIF-8, respectively. The results showed that the difference in modification position of MoS_2 QDs did not result in a significant current difference, which was further certified by current integration (b: 3.91×10^{-5} C, c: 4.26×10^{-5} C, and d: 4.33×10^{-5} C). In addition, ζ potential characterization proved the positive charge property of Lu/MoS_2 QDs@ZIF-8, which was beneficial to enrich luminol and $O_2^{\bullet-}$ to further improve the ECL efficiency (Figure 4B). As shown in Figure 4C, the obtained ECL intensities of Lu/GCE, Lu@ZIF-8/GCE, MoS_2 QDs/Lu@ZIF-8/GCE, MoS_2 QDs/Lu@ZIF-8/GCE, and Lu/MoS_2 QDs@ZIF-8/GCE were 1117, 1441, 2593, 5057, and 14 165 a.u., respectively. Conspicuously, combining the CV and ECL results, this distinct difference illustrated that when a similar number of electrons passed through the electrode, more $O_2^{\bullet-}$ was protected and participated in the ECL reaction to oxidize luminol$^{\bullet-}$ in Lu/MoS_2 QDs@ZIF-8 and remarkably improve ECL emission. Therefore, the calculated relative ECL efficiencies of luminol in MoS_2 QDs/Lu@ZIF-8/GCE, MoS_2 QDs/Lu/GCE, and Lu/MoS_2 QDs@ZIF-8/GCE were 2.58, 4.23, and 12.7 times that of Lu/GCE according to eqs S5−S7, respectively (Figure 4D).

Design Rationality Characterization of the Arched Region. Considering that arbitrarily lengthening sequences increased design complexity and even led to possible secondary hybridization reactions, an internal arched region in S1−S2 was introduced as a cushion area to coordinate structural stability and controllability. Hence, the length of the arched region in S1−S2 was optimized by designing alternative chains (N6−N10) as candidate chains for S1. As shown in Figure S11, when the arched-region length was more than 8 bases, the double-stranded S1−S2 cannot maintain the structural stability to ATP, and the ECL signal increased obviously; when the arched-region length was less than 8 bases, although the S1−S2 structure was very stable, it impeded the subsequent hybridization reaction of S2 and hindered the nucleic acid amplification efficiency. Therefore, N8 was finally selected as the S1 chain for subsequent experiments.

ECL Measurement of Fabricated Biosensors for miRNA-21. First, electrochemical impedance spectroscopy and ECL characterization probed the step-by-step process of sensor construction in Figure S12. Furthermore, as displayed in Figure S13, polyacrylamide gel electrophoresis was performed to prove the operation of the nucleic acid signal amplification strategy. After using a series of conditions in the optimization process including the H_2O_2 concentration, S1−S2 concentration, and reaction time (Figure S14), quantitative analysis of prepared biosensors for miRNA-21 was performed under optimal experimental conditions. As depicted in Figure S15, with the increase of miRNA-21 concentration (100 aM to 10 pM), the ECL signal elevated gradually, which presented a super-duper linear relationship with the logarithm of target miRNA-21 concentration. The regression equation of $I = 1511.6 \lg c + 26\,915.4$ was fitted with the squared correlation coefficient of $R^2 = 0.998$ and the low detection limit of 14.6 aM was further estimated, indicating the marvelous sensitivity of the proposed biosensor. In addition, the biosensor demonstrated marvelous stability and specificity toward miRNA-21 (Figure S16). We compared the biosensor proposed in this work with related work (Table S2). Compared with the recent detection strategies based on fluorescence,[33] surface-enhanced Raman scattering,[34] and electrochemical[35] techniques, the biosensor in this work shows obvious advantages in both detection range and detection limit. Significantly, the biosensors proposed in this work demonstrate higher detection sensitivity than other biosensors developed based on ECL technologies, such as the strategy based on gold nanorod vertical arrays and catalytic hair pin self-assembly[36] and the strategy based on entropy-driven strand displacement reaction and tetrahedral DNA nanostructures.[37]

Practical Detection of the Biosensors for Tumor Cell Lysates. For evaluating practicability of the developed biosensors to tumor samples, breast adenocarcinoma cells (MCF-7, highly expressed miRNA-21) and human cervical cancer cells (HeLa, poorly expressed miRNA-21) were cultured, followed by being counted and processed with a commercialized extraction kit. As revealed in Figure 5, ECL

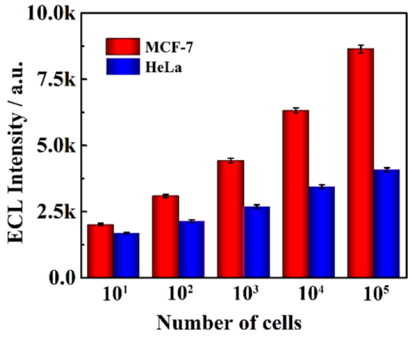

Figure 5. ECL responses of fabricated biosensors toward to miRNA-21 lysed from different numbers of MCF-7 and HeLa cells.

intensity responded sensitively to variation in MCF-7 number. However, a slow growth tendency was displayed when the biosensors were incubated with lysate of different concentrations of HeLa cells. The result of the experiment was not only consistent with previous works[38−41] but also showed practical applicability of proposed biosensors to miRNA-21 in cancer cells.

CONCLUSIONS

In this work, Lu/MoS_2 QDs@ZIF-8 was successfully prepared via in-site assembly of luminol into ZIF-8 by coordination linkage as well as the simultaneous encapsulation of MoS_2 QDs, in which luminol acted as a luminophor and MoS_2 QDs acted as a co-reaction accelerator, significantly improving the ECL intensity of the luminol−H_2O_2 system. Notably, porous Lu/MoS_2 QDs@ZIF-8 provided confined cavities to reduce the distance of the ternary system and greatly enhance the ECL efficiency. Moreover, positively charged Lu/MoS_2 QDs@ZIF-8 trended to confine more $O_2^{\bullet-}$ to further enhance the ECL intensity. As a consequence, Lu/MoS_2 QDs@ZIF-8 exhibited super-robust and stable ECL emission, which combined with the endogenous ATP-driven target recyclable nucleic acid

https://doi.org/10.1021/acs.analchem.2c01444
Anal. Chem. 2022, 94, 9106−9113

amplification tactic to achieve ultrasensitive monitoring of miRNA-21, validating the excellent practical applicability in ECL analysis. It can be reasonably predicted that the universal strategy for enhancing the ECL efficiency provides a promising prospect in detection of biomarkers and clinical diagnosis.

■ ASSOCIATED CONTENT

Supporting Information

The Supporting Information is available free of charge at https://pubs.acs.org/doi/10.1021/acs.analchem.2c01444.

Materials and reagents, apparatus, preparation of Pt nanoparticles, pretreatment of oligonucleotides, ζ potential characterization of luminol and Lu/MoS_2@ZIF-8, immobilization efficiency of luminol, regulating MoS_2 QD encapsulation quantity, immobilization efficiency of MoS_2 QDs, study for relative electrochemical surface areas, characterization for biosensor fabrication, polyacrylamide gel electrophoresis analysis, optimization of experimental conditions, and selectivity and stability characterization (PDF)

■ AUTHOR INFORMATION

Corresponding Authors

Yaqin Chai − *Key Laboratory of Luminescence Analysis and Molecular Sensing (Southwest University), Ministry of Education, College of Chemistry and Chemical Engineering, Southwest University, Chongqing 400715, PR China;* orcid.org/0000-0003-4392-9592; Phone: +86 23 68252277; Email: yqchai@swu.edu.cn; Fax: +86 23 68253172

Ruo Yuan − *Key Laboratory of Luminescence Analysis and Molecular Sensing (Southwest University), Ministry of Education, College of Chemistry and Chemical Engineering, Southwest University, Chongqing 400715, PR China;* orcid.org/0000-0003-3664-6236; Email: yuanruo@swu.edu.cn

Authors

Wei Liu − *Key Laboratory of Luminescence Analysis and Molecular Sensing (Southwest University), Ministry of Education, College of Chemistry and Chemical Engineering, Southwest University, Chongqing 400715, PR China*

Meiling Su − *Key Laboratory of Luminescence Analysis and Molecular Sensing (Southwest University), Ministry of Education, College of Chemistry and Chemical Engineering, Southwest University, Chongqing 400715, PR China*

Anyi Chen − *Key Laboratory of Luminescence Analysis and Molecular Sensing (Southwest University), Ministry of Education, College of Chemistry and Chemical Engineering, Southwest University, Chongqing 400715, PR China*

Kanfu Peng − *Department of Kidney, Southwest Hospital, The Third Military Medical University (Army Medical University), Chongqing 400038, China*

Complete contact information is available at: https://pubs.acs.org/10.1021/acs.analchem.2c01444

Notes

The authors declare no competing financial interest.

■ ACKNOWLEDGMENTS

This paper was financially supported by the National Natural Science Foundation of China (22174113, 21974108, and 22176153) and the Fundamental Research Funds for the Central Universities (XDJK2019TJ002), China.

■ REFERENCES

(1) Luo, R. G.; Lv, H. F.; Liao, Q. B.; Wang, N. N.; Yang, J. R.; Li, Y.; Xi, K.; Wu, X. J.; Ju, H. X.; Lei, J. P. *Nat. Commun.* **2021**, *12*, 6808.
(2) Peng, H.; Huang, Z.; Deng, H.; Wu, W.; Huang, K.; Li, Z.; Chen, W.; Liu, J. *Angew. Chem., Int. Ed.* **2020**, *59*, 9982−9985.
(3) Gao, T.-B.; Zhang, J.-J.; Wen, J.; Yang, X.-X.; Ma, H.-b.; Cao, D.-K.; Jiang, D. *Anal. Chem.* **2020**, *92*, 1268−1275.
(4) Wang, J.; Haghighatbin, M. A.; Shen, W.; Mi, L.; Cui, H. *Anal. Chem.* **2020**, *92*, 7062−7070.
(5) Zhang, P.; Ouyang, Y.; Willner, I. *Chem. Sci.* **2021**, *12*, 4810−4818.
(6) Duan, Y.; Song, Y.; Fan, N.; Yao, Y.; Deng, S.; Ding, S.; Shen, B.; Yin, Q. *Biosens. Bioelectron.* **2022**, *197*, 113784.
(7) Ling, J.; Zhao, M.; Chen, F.; Zhou, X.; Li, X.; Ding, S.; Tang, H. *Biosens. Bioelectron.* **2019**, *127*, 167−173.
(8) Saqib, M.; Bashir, S.; Li, H.; Li, C.; Wang, S.; Jin, Y. *Anal. Chem.* **2019**, *91*, 12517−12524.
(9) Zhang, Y.; Xu, J.; Zhou, S.; Zhu, L.; Lv, X.; Zhang, J.; Zhang, L.; Zhu, P.; Yu, J. *Anal. Chem.* **2020**, *92*, 3874−3881.
(10) Liu, W.; Chen, A.; Li, S.; Peng, K.; Chai, Y.; Yuan, R. *Anal. Chem.* **2019**, *91*, 1516−1523.
(11) Gu, W.; Wang, H.; Jiao, L.; Wu, Y.; Chen, Y.; Hu, L.; Gong, J.; Du, D.; Zhu, C. *Angew. Chem., Int. Ed.* **2020**, *59*, 3534−3538.
(12) Bushira, F. A.; Kitte, S. A.; Xu, C.; Li, H.; Zheng, L.; Wang, P.; Jin, Y. *Anal. Chem.* **2021**, *93*, 9949−9957.
(13) Liu, J.-L.; Yang, R.; Chai, Y.-Q.; Yuan, R. *Anal. Chem.* **2021**, *93*, 13334−13341.
(14) Guo, J.; Xie, M.; Du, P.; Liu, Y.; Lu, X. *Anal. Chem.* **2021**, *93*, 10619−10626.
(15) Zhou, Z.; Liu, X.; Yue, L.; Willner, I. *ACS Nano* **2018**, *12*, 10725−10735.
(16) An, B.; Zeng, L.; Jia, M.; Li, Z.; Lin, Z.; Song, Y.; Zhou, Y.; Cheng, J.; Wang, C.; Lin, W. *J. Am. Chem. Soc.* **2017**, *139*, 17747−17750.
(17) Li, C.-F.; Xie, L. J.; Zhao, J. W.; Gu, L. F.; Tang, H. B.; Zheng, L. R.; Li, G. R. *Angew. Chem., Int. Ed.* **2022**, *61*, No. e202116934.
(18) Wang, S.; Yao, W.; Lin, J.; Ding, Z.; Wang, X. *Angew. Chem., Int. Ed.* **2014**, *53*, 1034−1038.
(19) Liu, T.; Li, P.; Yao, N.; Cheng, G.; Chen, S.; Luo, W.; Yin, Y. *Angew. Chem., Int. Ed.* **2019**, *58*, 4679−4684.
(20) Liang, J.; Gao, S.; Liu, J.; et al. *Angew. Chem.* **2021**, *133*, 5481−5488.
(21) Zhai, F.; Guan, Y.; Zhu, B.; Chen, S.; He, R. *Anal. Chem.* **2021**, *93*, 12346−12352.
(22) Oishi, M.; Saito, K. *ACS Nano* **2020**, *14*, 3477−3489.
(23) Kong, L.; Kou, B.; Zhang, X.; Wang, D.; Yuan, Y.; Zhuo, Y.; Chai, Y.; Yuan, R. *Chem. Sci.* **2021**, *12*, 15953−15959.
(24) Ye, M.; Kong, Y.; Zhang, C.; Lv, Y.; Cheng, S.; Hou, D.; Xian, Y. *ACS Nano* **2021**, *15*, 14253−14262.
(25) Ma, P.-Q.; Liang, C.-P.; Zhang, H.-H.; Yin, B.-C.; Ye, B.-C. *Chem. Sci.* **2018**, *9*, 3299−3304.
(26) Liu, X.; Wang, X.; Ye, S.; Li, R.; Li, H. *ACS Appl. Mater. Interfaces* **2021**, *13*, 27825−27835.
(27) Luo, Y.; Fan, S.; Yu, W.; Wu, Z.; Cullen, D. A.; Liang, C.; Shi, J.; Su, C. *Adv. Mater.* **2018**, *30*, 1704576.
(28) Yucel, T.; Cebe, P.; Kaplan, D. L. *Adv. Funct. Mater.* **2011**, *21*, 779−785.
(29) Che, J.; Chan-Park, M. B. *Adv. Funct. Mater.* **2008**, *18*, 888−897.
(30) Gopalakrishnan, D.; Damien, D.; Shaijumon, M. M. *ACS Nano* **2014**, *8*, 5297−5303.
(31) Ren, X.; Pang, L.; Zhang, Y.; Ren, X.; Fan, H.; Liu, S. *J. Mater. Chem. A* **2015**, *3*, 10693−10697.
(32) Guo, J.; Xie, M.; Du, P.; Liu, Y.; Lu, X. *Anal. Chem.* **2021**, *93*, 10619−10626.

(33) Wang, X.; Wang, Y.; Chen, S.; Fu, P.; Lin, Y.; Ye, S.; Long, Y.; Gao, G.; Zheng, J. *Biosens. Bioelectron.* **2022**, *198*, 113849.
(34) Zhu, R.; Feng, H.; Li, Q.; Su, L.; Fu, Q.; Li, J.; Song, J.; Yang, H. *Angew. Chem., Int. Ed.* **2021**, *60*, 12560−12568.
(35) Zhou, H.; Zhang, J.; Li, B.; Liu, J.; Xu, J.-J.; Chen, H.-Y. *Anal. Chem.* **2021**, *93*, 6120−6127.
(36) Liang, Z.; Zhao, J.; Wang, P.; Nie, Y.; Xu, S.; Ma, Q. *Anal. Chem.* **2022**, *94*, 1221−1229.
(37) Yu, L.; Zhu, L.; Yan, M.; Feng, S.; Huang, J.; Yang, X. *Anal. Chem.* **2021**, *93*, 11809−11815.
(38) Liao, Y.; Huang, R.; Ma, Z.; Wu, Y.; Zhou, X.; Xing, D. *Anal. Chem.* **2014**, *86*, 4596−4604.
(39) Meng, T.; Jia, H.; An, S.; Wang, H.; Yang, X. J.; Zhang, Y. F. *Sens. Actuators, B* **2020**, *323*, 128621.
(40) Hao, Q.; Xu, Q.; Niu, S.; Ding, C.; Luo, X. *Anal. Chem.* **2021**, *93*, 10679−10687.
(41) Zhou, D.-M.; Du, W.-F.; Xi, Q.; Ge, J.; Jiang, J.-H. *Anal. Chem.* **2014**, *86*, 6763−6767.

https://doi.org/10.1021/acs.analchem.2c01444
Anal. Chem. 2022, 94, 9106−9113